Sensors & Actuators: A. Physical 398 (2026) 117355

Contents lists available at ScienceDirect

Sensors and Actuators: A. Physical

journal homepage: www.journals.elsevier.com/sensors-and-actuators-a-physical

Ultrabroadband single-wavelength dip in a high-sensitivity fiber Mach–Zehnder interferometer using a refractive-index-selected liquid core

Cheng-Ling Lee *, Yan-Han Lu, Wei-Jhou Chen, Yi-Chia Hsia, Ching-Hsiang Shih, Wen-Hsun Hsieh

Department of Electro-Optical Engineering, National United University, Miaoli 36003, Taiwan

ARTICLE INFO

Keywords:
Fiber Mach–Zehnder interferometer (FMZI)
Single-wavelength dip
Ultrabroadband
Free-spectral-range (FSR)
Refractive-index–selected liquid core
Hollow-core fiber (HCF)

ABSTRACT

We present a high-sensitivity fiber Mach–Zehnder interferometer (FMZI) that uses a refractive-index-selected liquid core to realize an ultrabroadband single-wavelength dip (λ_{single}) across 1250–1650 nm with an ultra-wide free spectral range (FSR) $\geq$ 400 nm (up to ~1000 nm). The device is formed by splicing a short hollow-core fiber (HCF) segment of length L_c(10 μm core) and filling it with a liquid of refractive index $n_D < n_{cl}$, which sets the modal effective-index difference and collapses the interference-fringe comb into a high-extinction dip at a deterministic wavelength within the measurement window. We further introduce closed-form, experimentally validated operating-point maps that link the fabrication and filling variables (L_c, n_D)to the spectral outcomes (λ_{single}, FSR), enabling on-demand placement of the single-wavelength dip and the target FSR. This single-wavelength-dip, large-FSR scheme removes fringe overlap and order ambiguity, allowing unambiguous demodulation. Experiments on several FMZI configurations confirm isolated single-wavelength-dip operation over 1250–1650 nm with strictly monotonic thermal redshifts; the dip's high-temperature sensitivity approaches + 20 nm / °C for n_D = 1.424.

1. Introduction

Fiber-optic interferometers produce periodic spectral fringe patterns due to phase differences between light paths, and they can detect minimal changes in sensed parameters via interference effects. By combining the inherent advantages of optical fibers (compact size, flexibility, EMI immunity, and remote operation) with interferometric resolution, these sensors have been widely used for many parameter measurements [1–5]. However, most fiber-optic interferometers generate conventional multi-fringe spectra that impose limitations: even when high-contrast fringes (>30 dB) are retained over a broad window (e.g., 1250–1650 nm), the free-spectral range (FSR) is often only a few to a few tens of nanometers [1–4,6–12], so fringes become densely spaced and readily overlap under broadband measurement. Large perturbations then induce fringe-order ambiguity (aliasing) once the phase shift exceeds one fringe period, and fringe crowding complicates demodulation and degrades dynamic-tracking performance [5,9,12]. For example, a methane sensor using the optical Vernier effect in two parallel Sagnac loops (1 PM-PCF reference arm and one methane-film-coated PM-PCF sensing arm) reported an average sensitivity of ~197.8 nm/%. However, its measured spectra remain multi-fringe (envelope-limited) rather than a single-wavelength dip across the band, so fringe overlap and order ambiguity can still arise over wide spans [7].

A practical way to avoid overlapping and ambiguity is to engineer the spectrum to contain a single-wavelength dip (or peak) across a measurement range. In grating-based devices, fiber Bragg gratings (FBGs) inherently produce a single Bragg peak that shifts with the sensed parameters, enabling straightforward wavelength tracking [13]. Across physical and chemical contexts, typical FBG sensitivities are generally on the order of 1.2–6.2 pm/με (strain) and 10–50 pm/°C (temperature) [14,15]. Accordingly, single-resonant long-period fiber gratings (LPFGs) have been designed to exhibit ultrabroadband stopbands together with a single, isolated resonance, thereby avoiding multi-fringe confusion [16]. An ultrathin cladding LPFG further enables widely tunable single-resonant responses while maintaining the single-wavelength-dip performance [17]. Despite this simplicity and single-peak (or dip) signal readout, the sensitivity is modest compared with interferometers. Coating materials can increase the FBG temperature sensitivity [18], and embedding the grating in a polymer matrix (e.g., PMMA) exploits large thermal expansion to further enhance sensitivity [19], but the

* Corresponding author.
E-mail address: cherry@nuu.edu.tw (C.-L. Lee).

https://doi.org/10.1016/j.sna.2025.117355
Received 29 August 2025; Received in revised form 15 November 2025; Accepted 30 November 2025
Available online 5 December 2025

improvements are limited. Likewise, a leaky-guided multimode fiber interferometer using refractive-index-matched coupling achieved widely tunable, ultra-sensitive behavior while operating with a single isolated notch, thus preventing spectral overlap under large shifts [20]. Taken together, these studies indicate that a single-wavelength dip, large-FSR spectrum can preserve interferometric sensitivity while delivering an unambiguous readout over a broad wavelength window, which directly motivates our design. This study presents a fiber-optic interferometer that utilizes a micro-segment of a hollow-core fiber (HCF) filled with a selected liquid to provide unambiguous spectral responses. HCFs are chosen because their hollow central core permits straightforward introduction of liquids/films and strong modal interaction. HCF segments spliced with standard SMF have enabled a variety of fiber-optic interferometers [3,5,12,21–25]. Recent work has advanced HCF configuration coated with CQDs@BiOBr, which strengthens the evanescent-field interaction. These devices achieved room-temperature triethylamine detection with picometer-per-ppm spectral shifts [21]. In parallel, an HCF-based Fabry–Perot humidity sensor using a femtosecond-laser-perforated G–PVA film, paired with a reference FP, leveraged the Vernier envelope to achieve a sensitivity of ~4.64 nm/%RH [22]. Another study, a liquid-filled, tapered hollow suspended dual-core fiber forms a directional coupler governed by the liquid's thermo-optic coefficient, yielding very high temperature sensitivity (up to 38.281 nm/°C over 20–26 °C) [23]. Nevertheless, the optical spectra of the studies above [3,5,12,21–25] still exhibit multi-fringe patterns rather than a wideband single dip, allowing for overlap between fringes and ambiguity in fringe order over wide spans. These representative HCF–SMF cascade structures motivate our goal here: to retain interferometric sensitivity while engineering a deterministic single-wavelength dip with an ultrawide free-spectral range and broadband placement across 1250–1650 nm.

The proposed HCF-based fiber Mach–Zehnder interferometer (FMZI) employs a refractive-index-selected liquid core to produce a single-wavelength dip across 1250–1650 nm. The device consists of an HCF micro-segment of length L_c(core ≈ 10 μm) spliced into SMF and filled with a liquid of refractive index $n_D < n_{cl}$, which sets the modal effective-index difference and yields an ultrawide free spectral range (FSR) ≥ 400 nm (up to ~1000 nm). We further derive and experimentally validate closed-form operating-point maps that link the fabrication/filling variables $(L_c, n_D)$to the spectral outcomes $(\lambda_{single}, \mathrm{FSR})$, enabling deterministic placement of the single notch anywhere in the O–L bands and providing a practical design tool transferable to other interferometric configurations. Proper pairing of L_c and n_D collapses the fringe comb into a high-extinction dip, suppressing fringe overlaps and order ambiguity while retaining interferometric sensitivity. Experiments on several liquid-core FMZI devices confirm isolated single-wavelength dip operation over 1250–1650 nm with strictly monotonic thermal redshifts; the dip temperature sensitivity approaches + 20 nm / °C at $n_D = 1.424$.

2. Principle

Fig. 1 illustrates the principle and schematic structure of the proposed single-wavelength-dip FMZI (S-FMZI). The device follows our previously published liquid-filled, leaky-guided FMZI architecture [5]. As shown in Fig. 1(a), light from the input single-mode fiber (SMF) first expands into a large-core hollow-core fiber (HCF, core ≈ 50 μm, length L), then propagates through a micro-core section HCF_c (core ≈ 10 μm, length L_c). In the cascaded-HCFs, the large-core section mainly expands the mode and partitions optical power between the liquid core and the silica cladding to set the two-arm power ratio. However, only the micro-core section L_c forms the interferometer. After filling the device with a liquid of refractive index n_D selected to match L_c, as shown in Fig. 1(b), the modal effective-index difference $|\Delta n_{eff}|$ is set so that it generates an FSR that exceeds the measurement window, thereby ensuring single-wavelength-dip operation and the notch that can be placed precisely within the window.

To quantify the RI–length matching rule, we start from the destructive-interference condition [5], as shown in Eq. (1), which fixes the dip wavelength λ^{m}_{min} via the modal effective-index difference $|\Delta n^{eff}|$ and the micro-segment length L_c.

$$\lambda^{m}_{min} = \frac{2}{2m+1}|\Delta n^{eff}|\cdot Lc \tag{1}$$

where $\Delta n^{eff} = n^{eff}_{cl} - n^{eff}_{co}$ represents the effective index difference between the cladding mode and the core-like modes, and λ is the wavelength of the light. The n^{eff}_{cl} and n^{eff}_{co} are the effective refractive indices of the cladding and core modes, respectively. m represents the order of the interference mode, and it is an integer. Because the core refractive index is slightly lower than that of the silica cladding ($n_D < n_{cl}$), the core-like mode is leaky-guided rather than truly guided. Its effective index is complex ($\mathrm{Im}\{n^{eff}_{co}\} \neq 0$), representing leaky loss into the cladding. The free spectral range (FSR) of the proposed S-FMZI is the wavelength difference between two successive interference dips or peaks. By utilizing the relationship of the interference phase difference, the FSR can be derived and expressed in Eq. (2) [5].

$$\mathrm{FSR} = |\lambda_1 - \lambda_2| = \frac{\lambda_1\lambda_2}{|\Delta n^{eff}|\cdot L_c} \tag{2}$$

where λ_1 and λ_2 represent the wavelengths of two adjacent interference dips for the interference. Eq. (2) shows that we can strategically reduce the optical path difference (OPD): $|\Delta n^{eff}|\cdot L_c$ to enhance the FSR for achieving the single-wavelength dip (λ_{single}) in an ultrabroadband range

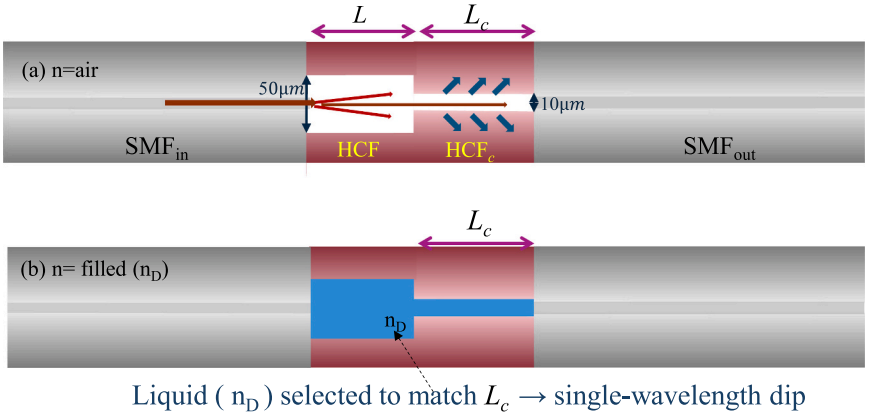

Fig. 1. (a) Schematic of the principle for the proposed S-FMZI with an air core (n = 1), used to calibrate the micro-segment length L_c. (b) After filling with a liquid of refractive index n_D selected to match L_c, the fiber device operates in the single-wavelength-dip regime and ultrawide FSR.

of measurement. To accomplish the λ_{single} operation over the 1250–1650 nm window, it is therefore equivalent to requiring FSR(λ_L) $\geq$ 400 nm, which bounds the needed refractive index contrast as shown below:

$$\left|\Delta n^{eff}\right| \leq \lambda_L^2 / (W \cdot Lc) \tag{3}$$

Here, λ_L represents the wavelength lower bound $\lambda_L = 1250$ nm, and W is the interrogation window width in our measurement range, with W $\geq$ 400 nm. It noted that in our study, the measurement window [λ_L, λ_H] had a width W$\equiv\lambda_H-\lambda_L$ (in our study λ_L=1250 nm, λ_H =1650 nm.)

For a fabricated S-FMZI with a fixed micro-segment length L_c, the most effective route to enforce single-dip operation is to reduce the modal effective-index difference Δn^{eff}. In practice—consistent with our ultracompact FMZI configuration [5]—this is achieved by filling the micro-core with a liquid whose refractive index n_D is lower than, yet close to the silica cladding refractive index n_{cl}, so that n_{co}^{eff} approaches n_{cl}^{eff}. For the 1250–1650 nm interrogation window (W=400 nm), we therefore require FSR $\geq$ 400 nm and the first minimum λ_{min} to fall within this range, 1250 nm < λ_{min} < 1650 nm.

Let two successive minima satisfy $\lambda_2 = \lambda_1$+FSR. Taking λ_1 to be the unique dip λ_{min} (hereafter denoted λ_{single}) and keeping the interferometric length at L_c, applying this relation to Eq. (2) yields the effective-index difference required for a target λ_{single}:

$$\left|\Delta n^{eff}\right| = \frac{\lambda_{single}\left(\lambda_{single} + FSR\right)}{FSR \cdot L_c} \tag{4}$$

Based on Eq. (4), we build a parameter-space diagram to analyze single-wavelength-dip operation. First, for each candidate liquid core (n_D = 1.30, 1.35, 1.395, 1.424), we compute the modal effective-index difference $|\Delta n^{eff}|(\lambda)$ over 1250–1650 nm with Sellmeier equations of the dispersion for n_{cl} [26] and Cauchy equation for the n_D [27]; these $\left|\Delta n_{eff}\right|$ appear as the solid curves. Because $n_D \lesssim n_{cl}$, the micro-segment supports a leaky core-like mode so n_{co}^{eff} is complex; for design simplicity we use $|\Delta n^{eff}| \approx n_{cl}^{eff} - \Re\{n_{co}^{eff}\} \approx n_{cl} - n_D$. For a fixed micro-segment length L_c, the right-hand side of Eq. (4) gives constant-FSR contours, plotted as dashed lines for target FSRs of

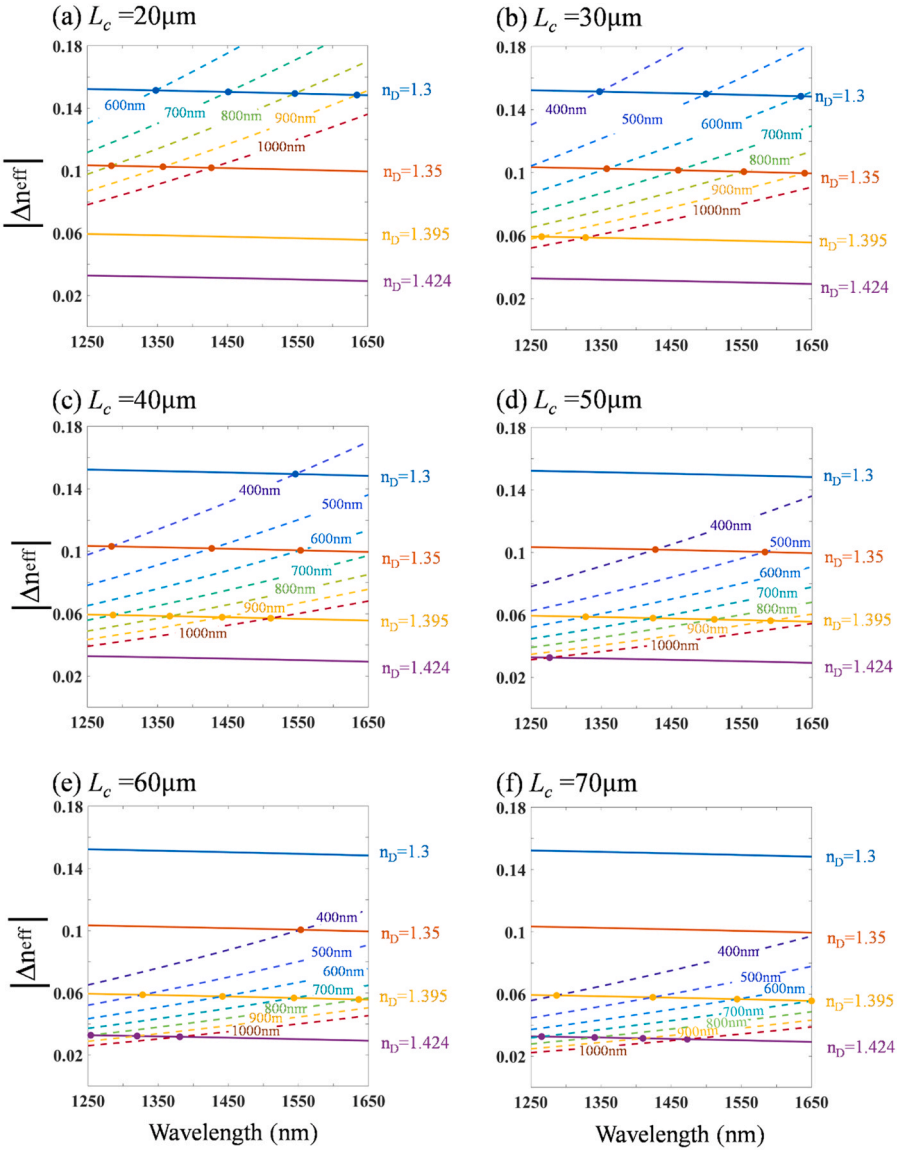

Fig. 2. Parameter-space diagrams at fixed micro-segment length L_c of (a) 20 μm, (b) 30 μm, (c) 40 μm, (d) 50 μm, (e) 60 μm, and (f) 70 μm, based on Eq. (4). Solid curves show the calculated $|\Delta n^{eff}|$ for liquid cores with n_D = 1.3, 1.35, 1.395, and 1.424 across 1250–1650 nm. Dashed curves are constant-FSR contours from 400 to 1000 nm in 100 nm steps. Intersections identify the admissible operating points (λ_{single}, FSR); points on the FSR contours guarantee single-wavelength-dip operation across the measurement window.

400–1000 nm in 100-nm steps. The intersection of a solid curve (chosen n_D) and a dashed contour (chosen FSR) defines an operating wavelength matched a (λ_{single}, $|\Delta n^{eff}|$) pair; the intersection's wavelength is the single-wavelength dip λ_{single} and the contour label is the device FSR. Repeating this for several L_c values produces the multi-panel diagram in Fig. 2(a–f). D

As an example, in Fig. 2(a) with $L_c = 20$ μm and $n_D = 1.30$, the intersections with the 600, 700, 800, and 900 nm contours give λ_{single} ≈ 1348, 1451, 1546, and 1635 nm, respectively. Hence, once L_c is known, the measured notch wavelength immediately reveals the device FSR by reading the corresponding dashed contour. In general, as L_c increases, Eq. (4) implies $|\Delta n^{eff}| \propto 1/L_c$; the same-FSR intersection therefore shifts toward higher n_D (smaller $|\Delta n^{eff}|$) and to longer λ_{single}. From Fig. 2(f), we also see that at $L_c = 70$ μm there is no intersection for $n_D = 1.30$ within 1250–1650 nm band, and $n_D > 1.35$ is required to realize single-wavelength-dip operation in this window. In all cases, intersections at or above the 400-nm contour guarantee the unique spectra across the 1250–1650 nm window. Because smaller $|\Delta n^{eff}|$ corresponds to larger FSR, the diagram predicts both the single wavelength λ_{single} and the resulting FSR for any (L_c, n_D) pair, enabling ultrabroadband single-wavelength-dip design.

Fig. 3 extends the parameter-space analysis of Fig. 2 by collapsing the intersections into $\lambda_{single}(L_c)$ positions within the 1250–1650 nm wavelength range (yellow region). Each panel fixes the FSR, and each line corresponds to a given liquid refractive index n_D. Thus, for a desired FSR (e.g., 400 nm), different (L_c, n_D) pairs place the single-wavelength-dip at different wavelength locations. For example, in Fig. 3(a), with L_c = 30μm and n_D= 1.3, the predicted λ_{single} is ~1348 nm; increasing to L_c = 40μm with the same n_D = 1.3 moves λ_{single} to ~1546.3 nm, whereas using n_D= 1.35 at L_c = 40μm yields λ_{single} is 1284.6 nm with FSR= 400 nm. These trends confirm that the plots can predict both the notch wavelength and the spectrum's FSR for a given (L_c, n_D) pair, enabling ultrabroadband single-wavelength dip design within the measurement window. Moreover, Fig. 3 shows that, for each liquid index n_D, the relation between λ_{single} and L_c is linear. Hence, the accessible wavelength range can be shifted upward or downward simply by scaling L_c: increasing L_c moves λ_{single} to longer wavelengths (slope set by n_D), whereas decreasing L_c would move it to shorter wavelengths. By choosing appropriate L_c, n_D pairs, the dip wavelength is set on demand while satisfying FSR ≥ 400 nm, yielding ultrabroadband single-wavelength dip spectra.

Based on the analysis above in Figs. 3–4, we developed a practical design tool that maps (L_c, n_D) to (λ_{single}, FSR), enabling the interferometer spectrum to realize, on demand, an ultra-wide FSR and a single-wavelength dip anywhere within the measurement window. Consequently, the proposed fiber device offers spectral characteristics well-suited for sensing applications. The single-wavelength dip can be arbitrarily positioned within the measurement wavelength band, suppressing fringe overlap and enabling ambiguity-free demodulation across the ultrabroadband window, thereby expanding the usable measurement range.

3. Fabrication and experimental results

The device was fabricated by sequentially fusion-splicing fibers: first a side-polished SMF (SPF) to a large-core HCF (HCF, core ≈ 50 μm, length L), then a short segment of small-core HCF (HCF_c), and finally a terminating SMF. All splicing was carried out on a Fujikura 90S fusion splicer under live monitoring, utilizing an optimized process to enhance yield. First, a side-polished SMF (SPF) was fused to a 50-μm-core HCF with pre-fusion standard−100 bit/240 ms, overlap 20 μm, first discharge −100 bit/100 ms, second, −100 bit/1 s (100 ms delay), then

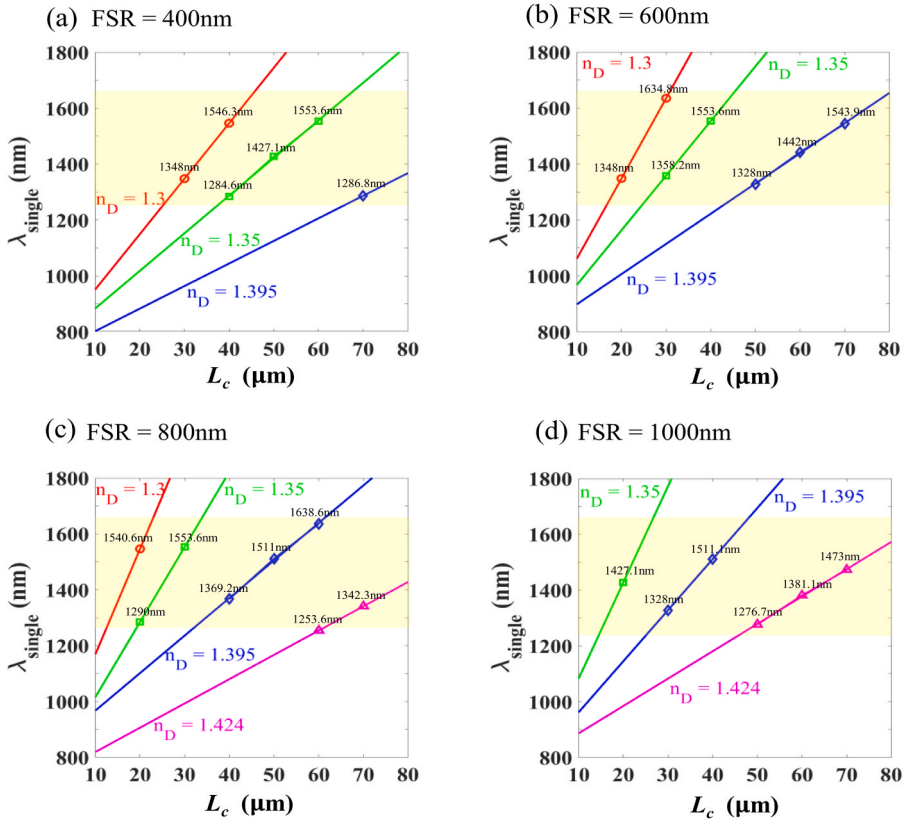

Fig. 3. Collections of λ_{single} versus L_c for selected n_D and desired FSR. (a)-(d) correspond to FSR= 400, 600, 800, and 1000 nm, respectively. Points are the intersections extracted from Fig. 2; lines are linear fits. The yellow shaded band marks the 1250–1650 nm measurement window. For a fixed FSR, longer L_c requires a higher n_D; increasing FSR shifts λ_{single} to longer wavelengths for all n_D.

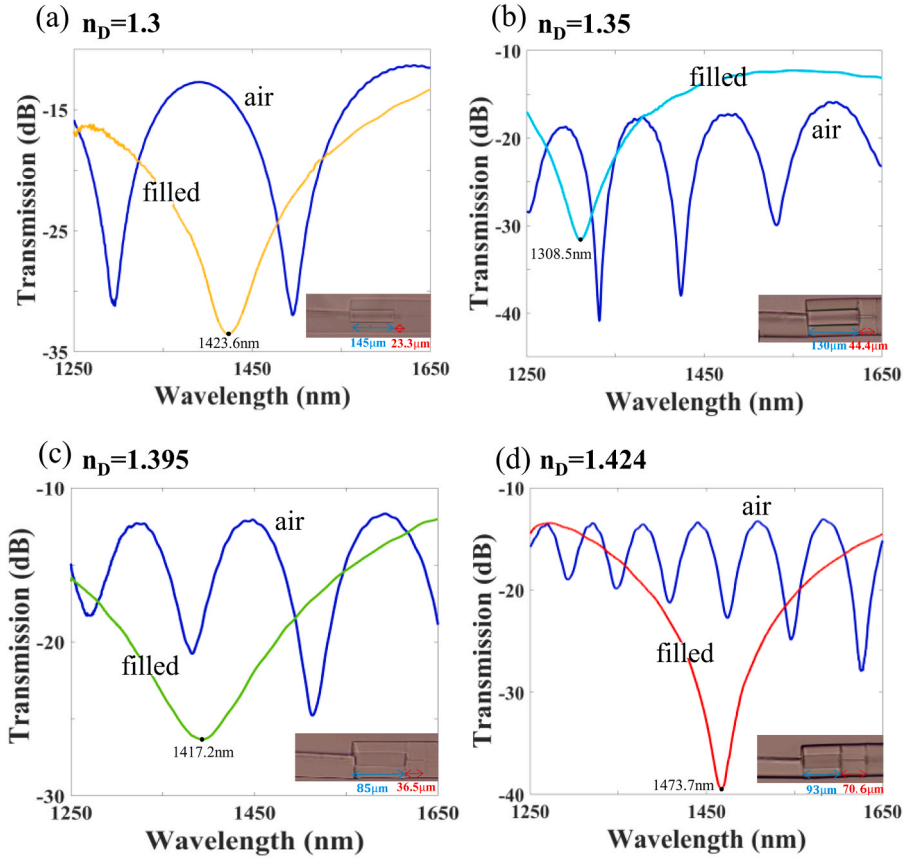

Fig. 4. Transmission spectra of four S-FMZIs over 1250–1650 nm. Blue: air-core baseline; colored: liquid-filled. Insets list front-HCF/micro-segment lengths L/Lc of (a) 145 μm / 23.3 μm, (b) 130 μm / 44.4 μm, (c) 85 μm / 36.5 μm, and (d) 93 μm/70.6 μm, respectively. With design liquids n_D= 1.3, 1.35, 1.395, and 1.424, the FSR exceeds 400 nm, and a single-wavelength dip appears at wavelengths of ≈ 1423.6, 1308.5, 1417.2, and 1473.7 nm at T = 25°C for (a)–(d), respectively.

the HCF was cleaved to the designed cavity length L. Here, the SPF's polished end face must be ~80–85 μm in width to create the microslit and to allow a stable fusion splice to the HCF. Next, the opposite end of this HCF was spliced to a 10-μm-core HCF_c with standard −60 bit/240 ms, overlap 10 μm, first + 0 bit/400 ms, second + 40 bit/1 s (100 ms delay), and the HCF_c was cleaved to the interferometric length L_c. Finally, the HCF_c was spliced to a standard SMF with standard −45 bit/240 ms, overlap 10 μm, first + 13 bit/400 ms, second + 76 bit/1000 ms (100 ms delay). It should be noted that, to prevent hollow-core collapse, the auto fusion-control was disabled, discharge power/duration were slightly reduced, and each joint used a small axial separation (≈10–20 μm overlap), yielding low-loss, repeatable splices. *("standard" denotes the splicer's built-in discharge level; 0 bit is the default.)* After constructing the cascaded SMF–HCF–HCF_c–SMF structure, a microslit at the junction is opened on the HCF; a microsyringe dispenses a small droplet at the microslit; capillary action draws the liquid into the hollow cores. Here, we used the Cargille refractive-index liquids with nominal n_D(589 nm, 25 °C) = 1.30, 1.35, 1.395, 1.424 (typical $dn/dT \approx -(3–5)\times 10^{-4}$ °C^{-1}). These values, together with the fused-silica Sellmeier model, were used to compute $|\Delta n^{eff}|$ and the operating-point maps. n this configuration, the large-core HCF acts as a beam splitter: it expands the optical field into both the HCF_c core and the silica cladding, balancing their intensities and enhancing the extinction ratio (ER). In contrast, the small-core HCF_c serves as the interference section, where leaky-guided core-like and cladding modes are excited when the liquid's refractive index is lower than that of the cladding. The corresponding lengths of HCF and HCF_c are denoted as L and L_c, respectively. For measurements, we launched a broadband light source (1250–1650 nm) into the input SMF and recorded the transmitted spectrum with an optical spectrum analyzer (OSA), while the device temperature was precisely controlled by a TE cooler (TEC). Under liquid-filled leaky-guided operation, the interferometer provides an ultrawide wavelength range with a single wavelength dip, avoiding fringe overlap and enabling unambiguous demodulation.

To validate the proposed mechanism for achieving an ultrawide wavelength range with a single-wavelength dip, we fabricated four S-FMZIs with different micro-segment lengths in the SMF-HCF-HCF_c-SMF configuration. We measured their transmission across 1250–1650 nm. For each device, the air-core spectrum was first recorded to calibrate its individual micro-segment length (L_c) from the measured FSR (using Eq. (2)). The device was then liquid-filled through the microslit with a Cargille optical liquid [5] of refractive index n_D selected to match the calibrated L_c. Fig. 4 displays the resulting spectra for four S-FMZIs with L_c = (a) 23.3μm, (b) 44.4μm, (c) 36.5μm, and (d) 70.6μm, filled with (at 25°C) n_D= 1.3, 1.35, 1.395, and 1.424, respectively. Fig. 4 shows that each device exhibits a single-wavelength dip within 1250–1650 nm, occurring at approximately 1423.6 nm (a), 1308.5 nm (b), 1417.2 nm (c), and 1473.7 nm (d), consistent with their designed (L_c, n_D) values. Because $n_D < n_{cl}$, the core-guided mode is leaky. Reducing $|\Delta n^{eff}|$ via Eq. (2) expands the FSR beyond 400 nm, leaving a single wavelength dip whose position is jointly determined by value of L_c and the selected n_D via Eq. (1). The insets of Fig. 4(a)–(d) show microscope images of the S-FMZI structures with L/L_c of (a) 145 μm / 23.3 μm, (b) 130 μm / 44.4 μm, (c) 85 μm / 36.5 μm, and (d) 93 μm / 70.6 μm, respectively. The corresponding air-core spectral responses exhibit clear interference fringes with multiple wavelength dips across 1250–1650 nm. As expected, a shorter L_c yields a wider fringe spacing (larger FSR), whereas the longest L_c in Fig. 4(d) produces the densest spectral fringes. After filling with the optical liquids, the FSR expands beyond the measurement window, and a single well-defined single-wavelength dip remains.

Increasing the micro-segment length (at fixed liquid) shifts the dip to longer wavelengths, while at fixed length, increasing the liquid's refractive index shifts the dip as predicted by the design diagrams in Fig. 2.

Table 1 summarizes the device geometries and single-dip operating metrics for the four S-FMZIs in Fig. 4(a)–(d). For each device, the micro-segment length L_c is measured and calibrated, and the liquid index n_D is selected accordingly. Using Eqs. (1)–(4), we predict the dip wavelength λ_{single} at 25 °C from the operating-point map (intersection of the solid $|\Delta n^{\text{eff}}|$ curve with the chosen constant-FSR contour). The interference order m is then obtained from the dip phase condition in Eq. (1). Number m is the integer that satisfies the destructive-interference condition at $\lambda_{\min}^{m} = \lambda_{\text{single}}$. Table 1 also lists the measured dip wavelength $\lambda_{\text{measured}}$ (25 °C) and the corresponding FSR (predicted). The measured $\lambda_{\text{measured}}$ agree with the predicted λ_{single} to within a few nanometers, and all predicted FSRs are ≥ 400 nm, confirming single-wavelength dip operation over the 1250–1650 nm window.

To verify single-wavelength dip operation under temperature modification, we measured the four liquid-filled S-FMZIs of Fig. 4 on the same BLS and OSA (operated at 0.8 nm resolution) measurement setup as the temperature varied from T = 15 °C to 35 °C under TEC control. In every case (Fig. 5(a)–(d), a single-wavelength dip is preserved across 1250–1650 nm, and it red-shifts monotonically as the temperature increases. No additional fringes appear because the FSR remains ≥ 400 nm at all temperatures, so the dip never overlaps a neighboring order, and the interference order m stays fixed. The initial wavelength dip positions at T = 25 °C follow the design results in Fig. 2-Fig. 4. For a given liquid, a longer micro-segment places the dip at a longer wavelength; for a given length, increasing the liquid refractive index shifts the dip as predicted. We can see in Fig. 5; the thermal responses are also governed by the thermo-optic coefficients of the two interference modes. As the thermal expansion of silica ($\sim 5\times10^{-7}$/°C) is two orders smaller than the thermo-optic terms and is neglected. The sensitivity can be written as the wavelength shift by temperature variation: $S = \frac{d\lambda_{\text{single}}}{dT}$ and expressed as the following approximation [5]

$$S \approx \lambda_{\text{single}} \cdot \frac{\frac{dn_{cl}}{dT} - \frac{dn_D}{dT}}{|\Delta n^{\text{eff}}|} \tag{5}$$

In our design, the temperature dependence of the refractive index of the silica and liquids are denoted by $\frac{dn_{cl}}{dT}$ and $\frac{dn_D}{dT}$, respectively. Since $\frac{dn_{cl}}{dT} > 0$, $\frac{dn_D}{dT} < 0$, and the $n_{\text{cl}} - n_D > 0$; Eq. (5) predicts $S > 0$; Therefore, the single-wavelength dip red-shifts as temperature increases. As n_D approaches n_{cl}, the effective-index contrast $|\Delta n^{\text{eff}}|$ decreases while the numerator in Eq. (5) stays positive, so S increases (stronger slope). Importantly, Fig. 5 demonstrates that the spectrum remains free of fringe overlap at all temperatures. The FSR stays ≥ 400 nm, so the dip can be directly read and demodulated unambiguously across the ultrabroadband range.

Fig. 6(a) plots the wavelength shift vs. temperature for the four liquid-filled S-FMZIs. In all cases, the single-wavelength dip red-shifts monotonically from 15 to 35 °C, and the sensitivity curve S(T) increases as the selected liquid index n_D approaches the cladding index n_{cl}. These trends agree with Eq. (5). Taking the local slopes of the fitted $\lambda(T)$ curves yield the temperature-dependent sensitivity $S(T)$ in Fig. 6 (b). Over this range, $S(T)$ rises approximately linearly, with a slight quadratic polynomial, indicating that the sensitivity considerably increases at higher temperatures. The markers at 25 °C give representative values: $S = 18.63$ nm/°C for $n_D = 1.424$, $S = 7.12$ nm/°C for $n_D = 1.395$, $S = 4.32$ nm/°C for $n_D = 1.35$, and $S = 3.18$ nm/°C for $n_D = 1.30$. The behavior presents the decrease of $|\Delta n^{\text{eff}}|$ as $n_D \to n_{cl}$, which enhances $S(T)$. During the measurement window, a single-wavelength dip is maintained (FSR ≥ 400 nm), so the response wavelength can be read directly without fringe overlap or order ambiguity. Moreover, using Eq. (5), we take $dn_{\text{cl}}/dT \approx +1 \times 10^{-5}$ °C^{-1} [27] for fused-silica cladding and $dn_D/dT \approx -(3 \sim 5) \times 10^{-4}$ °C^{-1} [26] for the selected Cargille liquids. At the D-line (589.3 nm), the four Cargille liquids used here have $n_D = 1.30$, 1.35, 1.395, and 1.424 with $\frac{dn_D}{dT} = -3.33\times10^{-4}$, -3.40×10^{-4}, -3.45×10^{-4}, and -4.02×10^{-4} °C^{-1}, respectively. Substituting these together with $|\Delta n^{\text{eff}}|(\lambda, n_D)$ solid curves from Fig. 2. that obtains the wavelength-dependent sensitivity $S(\lambda)$ at 25 °C for different n_D and they are shown in Fig. 6(c). We can see Eq. (5), $S(\lambda) \approx \lambda_{\text{single}} \cdot \frac{\frac{dn_{cl}}{dT} - \frac{dn_D}{dT}}{|\Delta n^{\text{eff}}|}$; it increases approximately linearly with wavelength (λ_{single}), i.e, longer wavelength dips are more thermally responsive. Moreover, with heating, the single dip red-shifts into a region of smaller $|\Delta n^{\text{eff}}|$, so the shift rate grows gradually. As different Cargille liquids used, the S also increases with the liquid refractive index n_D as $n_D \to n_{\text{cl}}$ and $|\Delta n^{\text{eff}}| \to 0$ to significantly enhance its S. Sampling the curves of Fig. 6(c) at each device's λ_{single} location yields sensitivities are marked about $S = 3.23$, 4.47, 8.69, and 19.4 nm/°C for the same $n_D = 1.30$, 1.35, 1.395, and 1.424, respectively. The results are in close agreement with the measurements in Fig. 6(b), further confirming the validity of this simplified model.

4. Conclusion

We have demonstrated a liquid-filled fiber Mach-Zehnder interferometer whose refractive-index-selected core and micro-segment length are co-designed to realize an ultrabroadband single-wavelength dip. By pairing L_c with a liquid index $n_D < n_{\text{cl}}$, the modal effective-index difference $|\Delta n^{\text{eff}}|$ is set so that the free-spectral range (FSR) exceeds the measurement window, even over 1000 nm. This single-wavelength-dip, large-FSR regime collapses the multi-fringe pattern into a single high-extinction notch, eliminating fringe overlaps and order ambiguity while preserving interferometric sensitivity. For the first time, a simple design rule was derived and expressed as operating-point maps that relate (L_c, n_D) to (λ_{single}, FSR). These maps deterministically place the λ_{single} dip anywhere in the O-L bands and predict the resulting FSR. Experiments on four devices validated the approach: after air-core segment L_c calibration, liquid filling with $n_D = 1.30$, 1.35, 1.395, and 1.424 produced isolated single-wavelength dip spectra at measurement ranges with all FSRs ≥ 400 nm (up to~1000 nm), in close agreement with the model. Thermal measurements from 15 °C to 35 °C preserved the single dip across the entire window and yielded strictly monotonic red shifts. The measured sensitivities agree with the calculated results for the four liquids, consistent with thermo-optic predictions. Based on a comprehensive study, the practical design tool that maps (L_c, n_D) to (λ_{single}, FSR) enables on-demand realization of an ultra-wide-FSR, single-wavelength-dip spectrum anywhere within the window. The developed S-FMZI, fully compatible with standard SMF, combines interferometric-level sensitivity with a clean, unambiguous single-dip readout over an ultrabroadband window, and should benefit a wide range of fiber-optic

Table 1
Device geometries and single-wavelength dip operating metrics for the S-FMZIs.

S-FMZI	L_c	n_D	λ_{single} (25°C)	$\lambda_{\text{measured}}$ (25°C)	FSR	m
(a)	23.3μm	1.3	1406 nm	1423.6 nm	~ 600nm	2
(b)	44.4μm	1.35	1306 nm	1308.5 nm	~ 400nm	3
(c)	36.5μm	1.395	1412.2 nm	1417.2 nm	~ 950nm	1
(d)	70.6μm	1.424	1463 nm	1473.7 nm	~ 1000nm	1

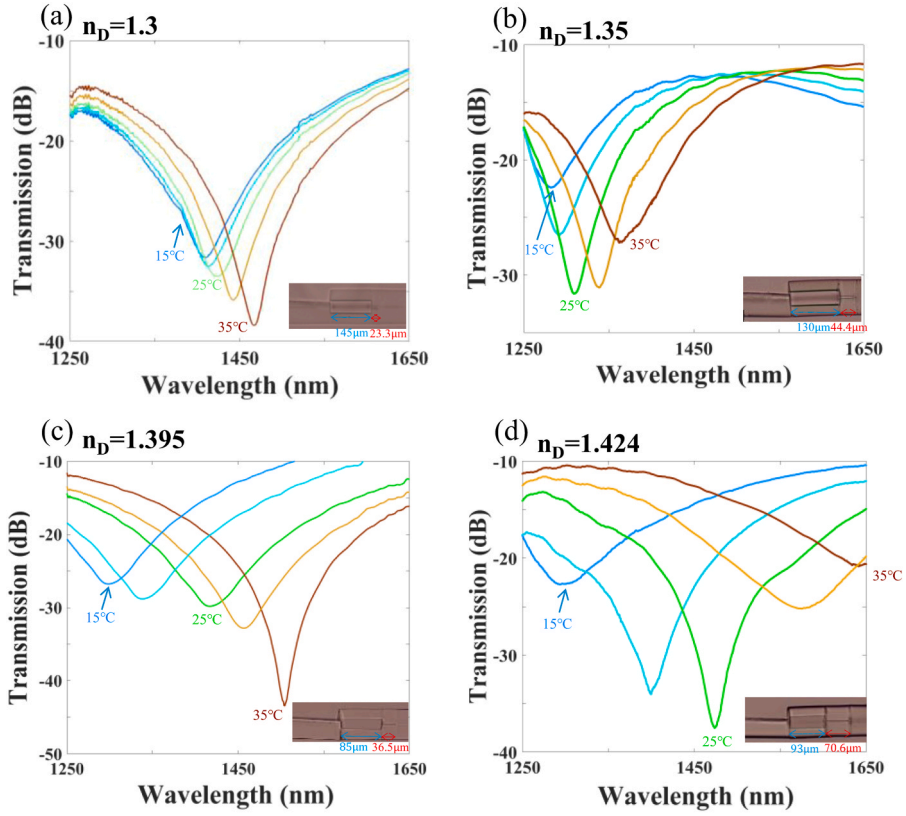

Fig. 5. The temperature responses of the liquid-filled S-FMZIs correspond to those in Fig. 4. Optical spectra were monitored as the temperature (T) was increased from 15 °C to 35 °C, indicating a single-wavelength dip maintained across 1250–1650 nm and a red shift with increasing temperature. Insets illustrate the corresponding micro-pictures. In all cases, the FSR remains ≥ 400 nm, so a single-wavelength dip is preserved across 1250–1650 nm.

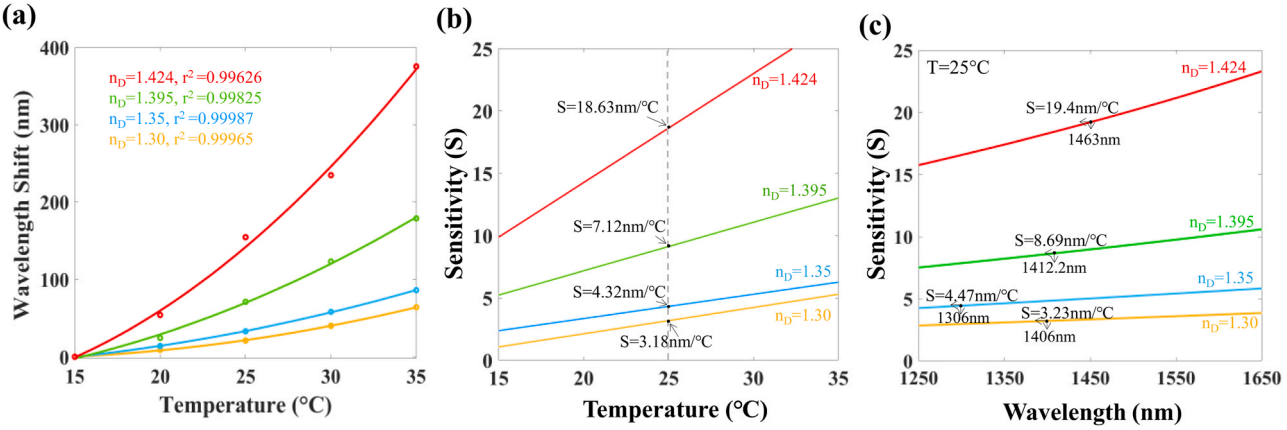

Fig. 6. Thermal responses of the S-FMZIs. (a) Measured single-wavelength dip (λ_{single}) shifts versus temperature (15–35°C) for liquids n_D = 1.30, 1.35, 1.395, and 1.424; solid curves are fits (shown with r^2). The λ_{single} red-shifts monotonically, with steep increasing as n_D approaches n_{cl} (b) Measured sensitivity $S(T) = d\lambda/dT$ obtained from the local slopes of the fitted curves in (a); markers at 25°C indicate 3.18, 4.32, 7.12, and 18.63 nm/°C for n_D = 1.30, 1.35, 1.395, and 1.424, respectively. (c) Theoretically predicted $S(\lambda)$ at 25 °C from Eq. (5) for the same n_D values. $S(\lambda)$ increases with wavelength and with n_D. For each device, the λ_{single} and its corresponding S are indicated.

sensing applications.

CRediT authorship contribution statement

Yi-Chia Hsia: Visualization, Data curation. **Wei-Jhou Chen:** Visualization, Software, Data curation. **Wen-Hsun Hsieh:** Visualization, Data curation. **Ching-Hsiang Shih:** Visualization, Data curation. **Yan-Han Lu:** Writing – original draft, Software. **Lee Cheng Ling:** Writing – review & editing, Validation, Supervision, Resources, Project administration, Methodology, Investigation, Funding acquisition, Formal analysis.

Declaration of Competing Interest

The authors declare that they have no known competing financial interests or personal relationships that could have appeared to influence the work reported in this paper.

Acknowledgments

This work was supported by the National Science and Technology Council of Taiwan, NSTC 113–2221-E-239–016.

Data availability

No data was used for the research described in the article.

References

[1] H. Zhang, S. Gao, Y. Luo, Z. Chen, S. Xiong, L. Wan, X. Huang, B. Huang, Y. Feng, M. He, W. Liu, Z. Chen, Z. Li, Ultrasensitive Mach–Zehnder interferometric temperature sensor based on liquid-filled D-shaped fiber cavity (Art), Sensors 18 (4) (Apr. 2018) 1239, https://doi.org/10.3390/s18041239.

[2] J. Zhou, Y. Sun, H. Liu, H. Li, Y. Wang, J. Jiang, D. Xu, J. Yao, The highly sensitive refractive index sensing of seawater based on a large lateral offset Mach–Zehnder interferometer (Art), Sensors 24 (12) (Jun. 2024) 3887, https://doi.org/10.3390/s24123887.

[3] C. Mao, B. Huang, Y. Wang, Y. Huang, L. Zhang, Y. Shao, Y. Wang, High-sensitivity gas pressure sensor based on hollow-core photonic bandgap fiber Mach–Zehnder interferometer, Opt. Express 26 (23) (Nov. 2018) 30108–30115, https://doi.org/10.1364/OE.26.030108.

[4] B. Sun, Y. Huang, S. Liu, C. Wang, J. He, C. Liao, G. Yin, J. Zhao, Y. Liu, J. Tang, J. Zhou, Y. Wang, Asymmetrical in-fiber Mach–Zehnder interferometer for curvature measurement, Opt. Express 23 (11) (Jun. 2015) 14596–14602, https://doi.org/10.1364/OE.23.014596.

[5] C.-L. Lee, C.-Y. Yeh, Y.-X. Jiang, Effective liquid-filled leaky-guided fiber mach-zehnder interferometer with a side-polished fiber, IEEE Sens. J. 25 (6) (2025) 9681–9688.

[6] J.M. Yan, A.L. Zhang, Q.H. Cheng, W. Li, C. Sun, High sensitivity open-cavity Mach–Zehnder interferometer based on no-core fiber for seawater salinity measurement (Art), Optik 227 (2021) 165954, https://doi.org/10.1016/j.ijleo.2020.165954.

[7] C. Liu, H. Li, H. Bai, C. Pei, K. Li, C. Yu, P.P. Shum, An ultra-high sensitivity methane gas sensor based on Vernier effect in two parallel optical fiber Sagnac loops (Art), Opt. Commun. 540 (Aug. 2023) 129509, https://doi.org/10.1016/j.optcom.2023.129509.

[8] Z. Lin, R. Lv, Y. Zhao, B. Zhou, X. Wang, Y. Zhou, and Q. Zhao, "High-sensitivity special open-cavity Mach–Zehnder structure for salinity measurement based on etched double-side hole fiber," Opt. Lett., vol. 46, no. 11, pp. 2714–2717,021.

[9] S.K. Al-Hayali, A.M. Salman, A.H. Al-Janabi, Low-cost high-sensitivity pH sensor based on a droplet-shaped single-mode fiber Mach–Zehnder interferometer (Art), Opt. Fiber Technol. 71 (Jul. 2022) 102944, https://doi.org/10.1016/j.yofte.2022.102944.

[10] H.K. Zheng, R.Q. Lv, Y. Zhao, R. Tong, Z.T. Lin, X.X. Wang, Y.F. Zhou, Q. Zhao, Multifunctional optical fiber sensor for simultaneous measurement of temperature and salinity, no. 23, Opt. Lett. 45 (Dec. 2020) 6631–6634, https://doi.org/10.1364/OL.409233.

[11] S. Zhang, Z. Shao, J. Liu, M. Zong, J. Shen, H. Gao, G. Wang, M. Huang, An optical fiber Fabry–Perot pressure sensor with optimized thin microbubble film shaping for sensitivity enhancement (Art), Coatings 10 (4) (Apr. 2020) 358, https://doi.org/10.3390/coatings10040358.

[12] C.-L. Lee, J.-T. Chao, Y.-Z. Huang, Y.-H. Wu, Y.-K. Chiu, W.-W. Hsiang, Ultrahigh sensitive liquid core fiber Mach–Zehnder interferometer using a low light absorption (Art), Opt. Laser Technol. 188 (2025) 112919, https://doi.org/10.1016/j.optlastec.2025.112919.

[13] A.N.D. Alhussein, M.R.T.M. Qaid, T. Agliullin, B. Valeev, O. Morozov, A. Sakhabutdinov, Fiber Bragg grating sensors: design, applications, and comparison with other sensing technologies (Art), Sensors 25 (7) (2025) 2289, https://doi.org/10.3390/s25072289.

[14] K. Yao, Q. Lin, Z. Jiang, N. Zhao, B. Tian, G.-D. Peng, Design and analysis of a combined FBG sensor for the measurement of three parameters, IEEE Trans. Instrum. Meas. 70 (2021) 1–10, https://doi.org/10.1109/TIM.2021.3066163.

[15] G. Kaur, R.S. Kaler, Sensitivity enhancement of FBG sensor for portlandite monitoring, Opt. Fiber Technol. 46 (Dec. 2018) 83–87, https://doi.org/10.1016/j.yofte.2018.09.017.

[16] C.-L. Lee, P. Han, Optimal design of single resonant and ultrabroadband long-period fiber grating filters (Art), Opt. Eng. 48 (8) (Aug. 2009) 080501, https://doi.org/10.1117/1.3194285.

[17] C.-L. Lee, P.-C. Wu, L.-W. Liu, Single resonant and widely tunable ultrathin cladding long-period fiber grating filters, Opt. Rev. 17 (Jan. 2010) 1–4, https://doi.org/10.1007/s10043-010-0001-z.

[18] V. Mishra, M. Lohar, A. Amphawan, Improvement in temperature sensitivity of FBG by coating of different materials, Optik 127 (2) (2016) 825–828, https://doi.org/10.1016/j.ijleo.2015.10.014.

[19] T. Allsop, R. Neal, K. Cook, D.J. Webb, I. Bennion, R. Neal, Temperature sensitivity of a fiber Bragg grating embedded in PMMA, Appl. Opt. 44 (29) (Oct. 2005) 5953–5958, https://doi.org/10.1364/AO.44.005953.

[20] C.-L. Lee, K.-H. Lin, Y.Y. Lin, J.-M. Hsu, Widely tunable and ultrasensitive leaky-guided multimode fiber interferometer based on refractive-index-matched coupling, Opt. Lett. 37 (3) (Feb. 2012) 302–304, https://doi.org/10.1364/OL.37.000302.

[21] Y.-N. Wang, J. Li, Z. Yuan, F. Meng, Optical fiber triethylamine room temperature gas sensor based on HMS platform with DFT calculation and experimental demonstration (Art), Appl. Surf. Sci. 705 (May 2025) 163495, https://doi.org/10.1016/j.apsusc.2025.163495.

[22] R.-J. Tong, S.-C. Wu, H.-N. Zheng, X. Li, F. Xia, Parallel Fabry–Perot type fiber optic humidity sensor with hollow core fiber filled G–PVA based on vernier effect (Art), Sens. Actuators A Phys. 384 (2025) 116221, https://doi.org/10.1016/j.sna.2025.116221.

[23] X. Li, S. Gao, J. Yang, P. Ye, Z. Zhu, P. Li, J. Shi, L. Yuan, C. Guan, High sensitivity temperature sensor based on directional coupler in a liquid-filled tapered hollow suspended dual-core fiber, J. Light. Technol. 42 (14) (Jul. 2024) 5048–5054, https://doi.org/10.1109/JLT.2024.3381787.

[24] Y. Lu, M. Han, J. Tian, Fiber-optic temperature sensor using a Fabry–Perot cavity filled with gas of variable pressure, IEEE Photonics Technol. Lett. 26 (8) (Apr. 2014) 757–760.

[25] M. Hou, F. Zhu, Y. Wang, Y. Wang, C. Liao, S. Liu, P. Lu, Antiresonant reflecting guidance mechanism in hollow-core fiber for gas pressure sensing, Opt. Express 24 (24) (2016) 27890–27898, https://doi.org/10.1364/OE.24.027890.

[26] H. Jeong, K. Oh, Theoretical analysis of cladding-mode waveguide dispersion and its effects on the spectra of long-period fiber grating, J. Light. Technol. 21 (2003) 1838–1845.

[27] "Refractive index liquids." Cargille Laboratories. https://www.cargille.com/refractive-index-liquids/ (accessed Aug. 1, 2025)..

Cheng-Ling Lee received the Ph.D. degree from the Institute of Electro-Optical Engineering, National Chiao Tung University, Hsinchu, Taiwan, in 2003. From 2004–2010, she was an Associate Professor with the Department of Electro-Optical Engineering, National United University (NUU), Miaoli, Taiwan, and she was promoted to Full Professor in 2011. Dr. Lee is the author of more than 50 peer-reviewed journal publications. In 2025, she was recognized as a Top 2 % global scientist (Stanford–Elsevier list of global scientific impact). Her research interests include fiber-based devices, optical fiber sensors, all-fiber interferometers, and optical fiber waveguides.

Yan-Han Lu was born in 2002. He is currently pursuing the M. S. degree in Electro-Optical Engineering at National United University, Miaoli, Taiwan. His research interests include optical waveguide simulation with Rsoft commercial software, fiber-based devices, optical fiber sensors, and all-fiber interferometers.

Wei-Jhou Chen was born in 2005. He is currently a senior student in the B.S. program in Electro-Optical Engineering at National United University, Miaoli, Taiwan. His research interests include the fabrication and design of fiber-based devices, optical fiber sensors, and all-fiber interferometers.

Yi Chia Hsia was born in 2004 and is currently an undergraduate student at Electro-Optical Engineering, National United University in Miaoli, Taiwan. Her research interests include fiber-optic sensors, as well as chemical and biological experiments.

Ching-Hsiang Shih was born in 2005. He is currently an undergraduate student at Electro-Optical Engineering at National United University, Miaoli, Taiwan. His research interests include the fabrication of fiber-optic sensors, as well as chemical and biological experiments.

Wen-Hsun Hsieh was born in 2002. He is currently pursuing the M.S. degree in Electro-Optical Engineering at National United University, Miaoli, Taiwan. His research interests include the fabrication and design of fiber-based devices, and fiber-optic hot-wire anemometers.